Nuclear Engineering and Technology 55 (2023) 2018–2025

Contents lists available at ScienceDirect

Nuclear Engineering and Technology

journal homepage: www.elsevier.com/locate/net

Original Article

Experiment of proof-of-principle on prompt gamma-positron emission tomography (PG-PET) system for *in-vivo* dose distribution verification in proton therapy

Bo-Wi Cheon [a], Hyun Cheol Lee [b], Sei Hwan You [c], Hee Seo [d], Chul Hee Min [a, **], Hyun Joon Choi [c, *]

[a] Department of Radiation Convergence Engineering, Yonsei University, 26493, Wonju, South Korea
[b] Nuclear Materials Analysis Team, Korea Institute of Nuclear Nonproliferation and Control, Daejeon, 34054, South Korea
[c] Department of Radiation Oncology, Wonju Severance Christian Hospital, Yonsei University Wonju College of Medicine, Wonju, South Korea
[d] Department of Quantum System Engineering, Jeonbuk National University, Jeonju, South Korea

ARTICLE INFO

Article history:
Received 4 October 2022
Received in revised form
2 March 2023
Accepted 2 March 2023
Available online 4 March 2023

Keywords:
Proton therapy
Prompt gamma
Positron emission tomography
In vivo dose verification
Experiment
Detector

ABSTRACT

In our previous study, we proposed an integrated PG-PET-based imaging method to increase the prediction accuracy for patient dose distributions. The purpose of the present study is to experimentally validate the feasibility of the PG-PET system. Based on the detector geometry optimized in the previous study, we constructed a dual-head PG-PET system consisting of a 16 × 16 GAGG scintillator and KETEK SiPM arrays, $BaSO_4$ reflectors, and an 8 × 8 parallel-hole tungsten collimator. The performance of this system as equipped with a proof of principle, we measured the PG and positron emission (PE) distributions from a 3 × 6 × 10 cm^3 PMMA phantom for a 45 MeV proton beam. The measured depth was about 17 mm and the expected depth was 16 mm in the computation simulation under the same conditions as the measurements. In the comparison result, we can find a 1 mm difference between computation simulation and measurement. In this study, our results show the feasibility of the PG-PET system for in-vivo range verification. However, further study should be followed with the consideration of the typical measurement conditions in the clinic application.

1. Introduction

The goal of radiation therapy is to deliver the maximum dose to the tumour while sparing as much of the surrounding normal tissue as possible. Compared with photon therapy that could delivers an unnecessary dose to an extensive region of normal tissue [1–4], proton therapy has the potential benefit of sparing normal tissue with the characteristic dose distribution called as Bragg peak [5].

The initial kinetic energy of the proton beam determines the beam range. However, the uncertainty of the proton beam range in patients could be critical in accurately delivering the dose to target volume and sparing normal tissues, due to the steep dose gradient at the distal edge of the Bragg peak [6]. For this reason, treatment plans rarely are established using a single-field plan, even though the conformal dose distribution can be realized. On the other hand, intensity-modulated proton therapy, or techniques that patch the lateral single-field and distal fall-offs, may will be employed to reduce such risks. However, these techniques can deliver a relatively high dose to normal tissues and have concerns that are still highly sensitive to range errors [8]. Therefore, accurate prediction of *in-vivo* proton dose distribution in the human body is particularly important to improve treatment quality.

Various direct and indirect methods for in-vivo range verification have been proposed in particle therapy [6]. Among them, the prompt gamma (PG) [9–16] and positron emission tomography (PET) [17–25] is the most feasible representative technique that can indirectly predict the dose fall-off region by measuring the secondary radiation generated by the interaction between the proton beam and the patient's body.

Even though the prompt gamma measurement technique has the advantage of being able to accurately predict the point of a dose fall-off region in the depth direction and can monitor the patient's

* Corresponding author.
** Corresponding author.
E-mail addresses: chmin@yonsei.ac.kr (C.H. Min), hjchoi1@yonsei.ac.kr (H.J. Choi).

https://doi.org/10.1016/j.net.2023.03.004

dose in real-time during treatment, it has a limitation that obtaining a three-dimensional (3-D) dose distribution because the PG imaging technique has been studied for, mostly, the purpose of proton range estimation with a one dimensional gamma detection system. On the other hand, the PET imaging technique with high detection sensitivity could be a practical approach for 3-D estimation of the dose distribution. However, the distribution of proton-induced positron emitters (PE) has a relatively poor relationship with the dose distribution, therefore, the PET measurements have to be compared with predicted activity distribution or other reference images for treatment verification [25]. To overcome these limitations, we have proposed a PG-PET system that combines the advantages of PG and PET imaging methods and complementarily estimates 3-D dose distribution [26]. During proton beam irradiation, the proposed PG-PET system measures the PG distribution using multiple detector modules comprised of a 2-D parallel-hole collimator and a pixelated scintillator-based detector positioned at various angles. After the beam irradiation is turned off, the PG-PET system immediately starts measuring the PE distribution, without the collimators. In our previous study above-noted, the Monte Carlo (MC) method was employed to design and optimize the PG-PET system, and several background reduction techniques were suggested for clear verification of 3-D dose distribution in a water phantom.

The purpose of the present study is to experimentally validate the feasibility of the PG-PET system. Based on the detector geometry optimized in the previous MC study, we manufactured a dual-head PG-PET system. For a proof-of-principle study of the system, we measured PG and PE distributions with a PMMA phantom for a 45 MeV proton beam.

2. Materials and methods

2.1. PG-PET system

2.1.1. SiPM-based GAGG detector and parallel-hole collimator

A dual-head PG-PET system was manufactured for proof-of-principle purposes based on our previous optimization study using the MC method. A detector module comprises a $Gd_3Al_2Ga_3O_{12}$:Ce (GAGG:Ce) scintillator encapsulated with a Barium sulphate ($BaSO_4$) reflector coupled with a silicon photomultiplier (SiPM) and a parallel-hole tungsten collimator. A 2-D array GAGG:Ce scintillator was made by C&A Corporation (Sendai, Miyagi, Japan). The $63.7 \times 63.7 \times 30$ mm^3 scintillator array is composed of a 16×16 array of $3.3 \times 3.3 \times 30$ mm^3 unit scintillators at 4 mm intervals. Between the unit scintillators, a 0.7 mm-thick $BaSO_4$ reflector is filled in a lattice form and a 0.2 mm-thick $BaSO_4$ reflector surrounds the outside of the scintillator array (Fig. 1). Based on the geometry of the GAGG:Ce scintillator array, a SiPM array (model: PA3315-WB-1608) was customized by KETEK GmbH Electric Corporation (Munich, Germany). The SiPM array consists of an 8×16 array of 3×3 mm^2 SiPM pixels at 4 mm intervals (Fig. 1). The size of the SiPM pixels is slightly smaller than that of the unit scintillator in order to minimize interference from the lights generated by the adjacent scintillators. Each SiPM pixel consists of 38,800 15 μm-size microcells. The breakdown voltage and over-voltage for SiPM array operation were set by the manufacturer's recommendation as 27V and 5V, respectively. TSK-5353 optical grease was used to bridge the gap (or boundary) of light signals between the scintillator and SiPM, thus increasing the transfer capability of the light signals. Finally, a 16×16 GAGG scintillators, four 8×16 SiPM arrays, and optical grease were used to construct a gamma detection module combined as a dual-ended readout module that collects light signals at both ends of the scintillator array (Fig. 1). The dual-ended readout system was manufactured as a total of two sets to apply to the dual-head PG-PET system.

An 8×8 parallel-hole tungsten collimator for measuring PG distribution was constructed by using two types of tungsten plates and a plastic frame. One tungsten plate is a simple plate $1 \times 68 \times 200$ mm^3 in size, while the other is $1 \times 68 \times 205$ mm^3 in size, with seven 1.15×200 mm^2 grooves located at 8 mm intervals. The plastic frame has seven 2 mm grooves spaced at 8 mm intervals. The tungsten plates are inserted into the plastic frame to create the lattice form (Fig. 2).

2.1.2. Data acquisition system

Multi-channel signals were processed by using an application-specific integrated circuit (ASIC)-based data acquisition (DAQ) system, in consideration of its compact size, expendability, and fast processing speed. An ASIC is a circuit designed for a specific purpose by removing unnecessary functions and has the advantages of high processing speed, miniaturization, scalability, and versatility of signal processing circuits [27], When the light emitted from a scintillator reaches a SiPM pixel, it is transformed into an electrical analogue signal. A signal processing circuit receives the analogue signal from the SiPM pixel and determines whether it has to be considered or not in the PG or PE analysis. The signal is then digitized and transmitted to a computer for analysis.

In this study, we employed sixteen TOFPET2 64-channel ASICs [28] made by PETsys Electronics (Oeiras, Portugal) in order to process a total of 1024-channel signals measured by the dual-head PG-PET system. A single 8×16 SiPM array (PA3315-WB-1608) was connected to a front-end module (FEM) equipped with two TOFPET2 ASIC chips. A total of eight FEM-SiPM array sets (1024 channels) were connected to a front-end-board type D (FEB/D) equipped with a Kintex 7 field programmable gate array (Fig. 3). Through the FEM, multiple signals were processed by amplifying the signal and classifying its energy and timing data into multiple pre-set signal processing parameters. Next, 1024-channel signals were integrated into the FEB/D and transmitted to the computer through 1 Gbps Ethernet communication using a CAT6 LAN cable. The signal data was stored in the computer in a list-mode that provided the channel number, energy in nanocoulomb (nC) units, and time in picosecond (ps) units. The accumulated data was stored for a specific measuring time, and analyzed and processed to obtain a projection image of the gamma emission distribution.

2.1.3. Dual-head PG-PET with cooling system

A pair of multi-channel GAGG scintillation detectors capable of measuring both PG and PE distributions were constructed, as illustrated in Fig. 4. Each detector could measure the interaction position of the incident gammas in 16×16 positions (256 channels), and both ends of the GAGG scintillator through the four FEM could process a total of 512-channel signals. We used a HLCD-40-10-00-BD-BH-1 cable to connect two different types of printed circuit boards of the FEM to minimize the obstructive factor for incidental gammas caused by the shape of the FEM. Each FEM had two ASIC chips.

The cooling system was constructed in the PG-PET system to reduce the electrical noise resulting from the high temperature. The customized heat sink was manufactured based on the structural information of the ASIC chip mounted on the FEM. A small fan cooled the heat sink combined with the FEM in the detector housing. The air-cooling function was intensified by using an aluminium box equipped with Peltier elements that cooled the air inside the box. Thereby, ASIC cooling was almost constantly

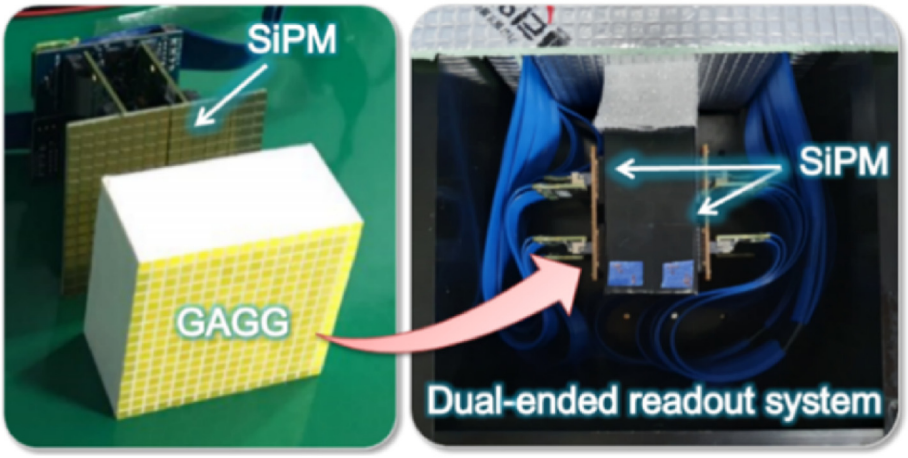

Fig. 1. A gamma detection module combined using a 16 × 16 GAGG:Ce scintillator and customized four 8 × 16 SiPM arrays as a dual-ended readout module.

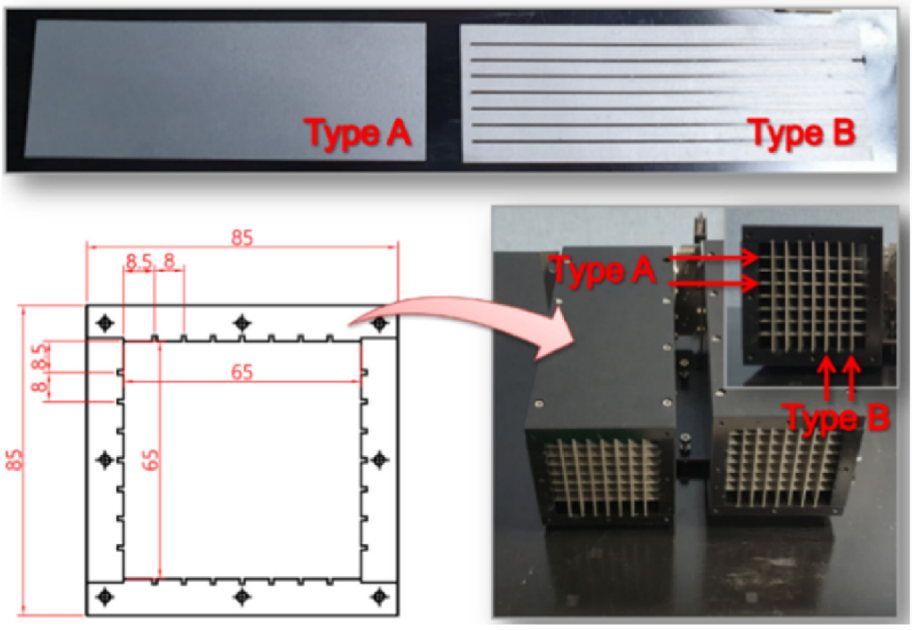

Fig. 2. Two parallel-hole collimators where two types of tungsten plates were combined in a lattice form on a plastic frame.

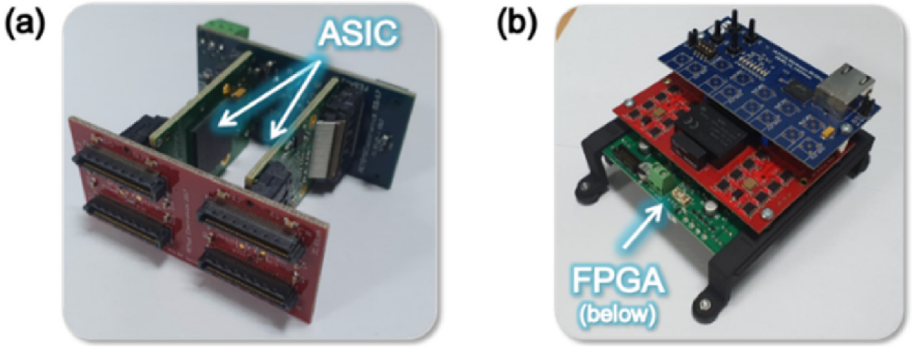

Fig. 3. (a) Front-end module (FEM) equipped with two TOFPET2 application specific integrated circuit (ASIC) chips, (b) front-end-board type D (FEB/D) equipped with Kintex 7 field programmable gate array.

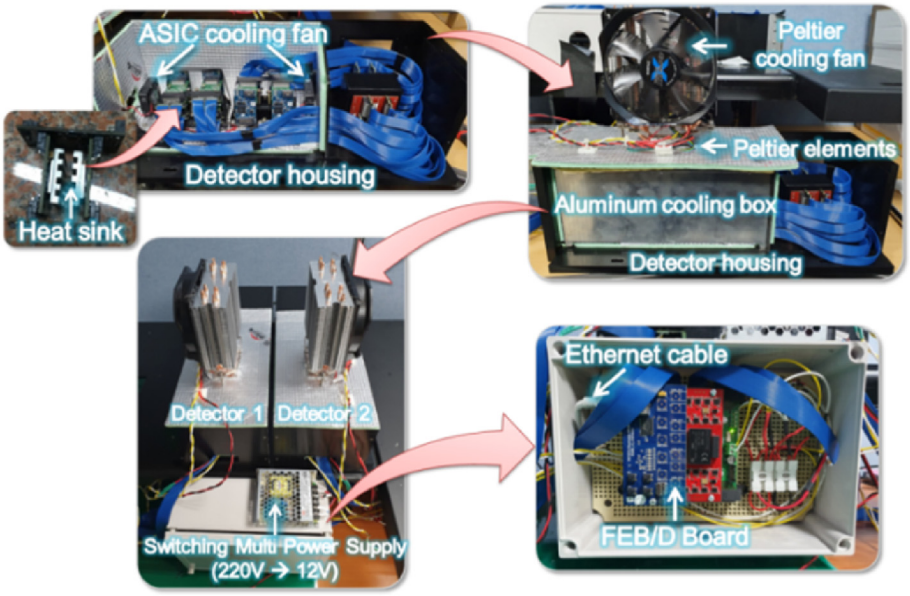

Fig. 4. Dual-head PG-PET system equipped with TOFPET2 ASIC-based data acquisition system and cooling system.

maintained. The Peltier elements were cooled using a commercially available large fan as illustrated in Fig. 4. A switching multi-power supply was employed to operate all of them simultaneously.

2.2. Performance evaluation of dual-head PG-PET system using test sources

The performance of the proposed PG-PET system was evaluated for gamma energies of 356, 511, 662, and 1275 keV. The ^{133}Ba, ^{22}Na, and ^{137}Cs sources were placed 410 mm from each detector surface (i.e., about six times farther than the length of a detector). The energy spectrum for each channel was measured at different times, depending on the radioactivity of the four test sources. The energy resolution was evaluated according to the full width at half maximum (FWHM) of the peak of the Gaussian fitting curve on each energy spectrum. In addition, the sensitivity for each channel was evaluated by summing the detected counts in the energy range of the FWHM of the peak. Variations of sensitivity for each channel were obtained using a 38.5 μCi ^{137}Cs source over 3 h of measurement.

2.3. Acquisition of PG-PET images for 45 MeV proton beam

An experimental study to verify the proton dose distribution was performed at the Korea Institute of Radiological and Medical Sciences (KIRAMS). A 45 MeV proton beam with a 1 nA current generated by an MC-50 cyclotron was irradiated to a $30 \times 60 \times 100$ mm^2 PMMA phantom to measure the PG and PE distributions emitting from the phantom. Fig. 5 shows the experimental setup. The pair of PG-PET detectors faced each other. The surface of each collimator and the center of the scintillator were 11 cm and 37.6 cm from the center of the PMMA phantom, respectively. A 10 cm-thick lead block for each detector was placed next to the collimator and in front of the detector, housing to protect the ASIC chips from background radiation generated by the PMMA phantom. A 15 cm-thick lead block was placed behind the PMMA phantom, in the proton beam direction, to protect the FEB/D board from the significant amount of radiation generated by both the beam nozzle and the PMMA phantom.

The proton dose distribution was measured using EBT3 model Gafchromic films by irradiating the beam for 200 s. The PG distributions were obtained when the proton beam was turned on for 10 s (6.25×10^{10} protons) for the two different positions of the PMMA phantom. The first PMMA phantom position was set at the center of the collimator and the next position was the edge to the beam nozzle side of the collimator. After measuring the PG distributions, the collimators were disassembled from the detector modules, and then the coincidence projection images of 511 keV gammas emitted near the PE was obtained for 1000 s immediately after 500 s of beam irradiation. The coincidence projection images were reconstructed using a maximum-likelihood expectation maximization (MLEM) algorithm implemented in Customizable and Advanced Software for Tomographic Reconstruction (CASToR) version 2.1, an open-source C++ parallel platform [29]. For PET image reconstruction, the sub-set and the number of interactions were 5 times, respectively.

3. Results and discussions

3.1. Performance evaluation using test sources

The performance of the proposed PG-PET system was evaluated for gamma energies of 356, 511, 662, and 1275 keV. As shown in Table 1, the performance evaluation shows the mean energy resolutions and standard deviations of the energy spectra as measured in the scintillator pixels of each detector for four gamma energies. According to each energy, the mean energy resolution was evaluated at15.4%, 12.7%, 11.4%, and 3.5% on detector 1, and the higher the energy, the better the energy resolution was evaluated. In addition, the standard deviation was evaluated to be about 3%. The mean energy resolution of detector 1 was about 2% better than that of detector 2. Regarding the sensitivity variations for every scintillator pixel, the standard deviations of peak counts of detector 1 and detector 2 were 12% and 24%, respectively.

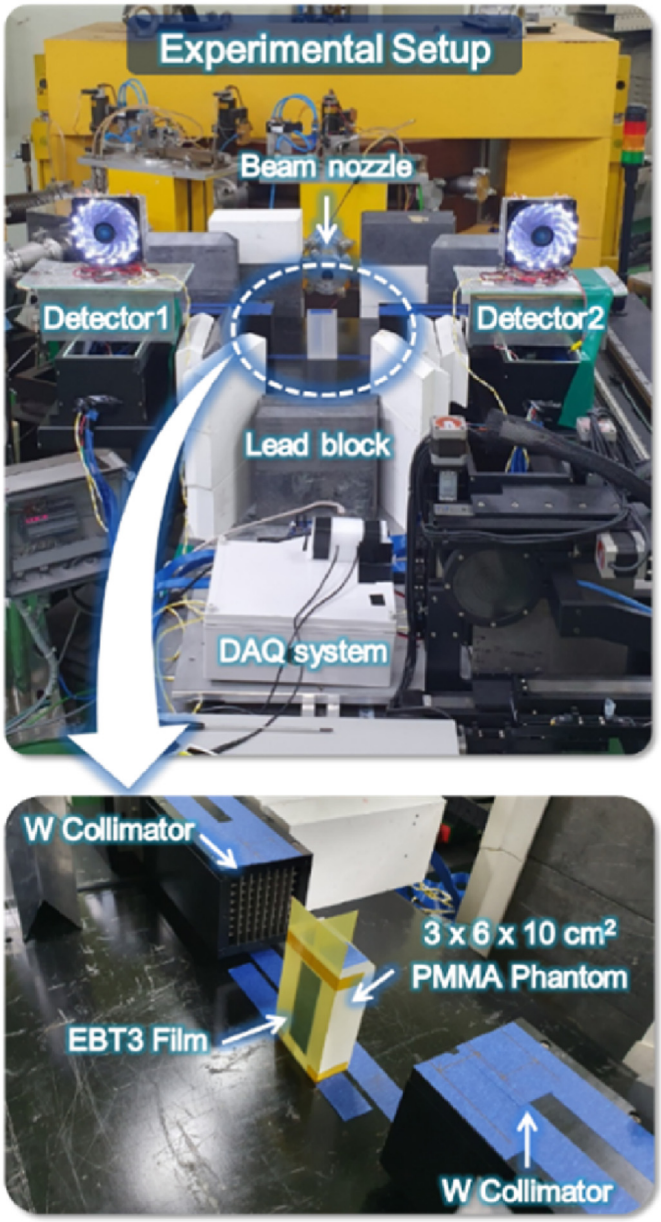

Fig. 5. Experimental setup at Korea Institute of Radiological and Medical Sciences for imaging performance test of PG-PET system as proof of principle.

3.2. Acquisition of PG-PET images for 45 MeV proton beam

3.2.1. Proton dose distribution

Dose distribution measurements using EBT3 films indicated that the 45 MeV proton range of maximum dose in the PMMA phantom was 17 mm (Fig. 6 (a)), which was predicted by the MC method using Geant4.10.00. p02 (Fig. 7 (a)). For the MC simulation, the range cut value of gamma and electrons was set as 100 μm and the physics model was set to QGSP_BIC_HP_EMY [30]. The characteristics of the secondary radiations emitted by a 30 × 60 × 100 mm^2 PMMA phantom by interaction with a 45 MeV proton beam were analyzed. PG evaluated the number of gammas generated by the inelastic reaction of protons with the PMMA phantom, and each PE nuclide was evaluated assuming that PE generated 500 s after proton beam irradiation was calculated for about 1000 s. Regarding the depth dose distribution, as the depth increased, the dose distribution spread out. The shape of the lateral dose distribution was an inclined oval shape of 20 mm in diameter (Fig. 6 (b)), and the calculated diameter by the MC method was about 17 mm (Fig. 7 (b)). Considering the difference in photosensitivity of EBT3 film, the actual measurement showed a difference of about 3 mm in diameter. The width of the lateral dose distribution was the longest in the region slightly above the center of the dose distribution, and it tended to shorten in the outer region.

3.2.2. Prompt gamma (PG) distribution

For a proof-of-principle experiment, the PG distributions for the 45 MeV proton beam were obtained in two different PMMA phantom positions. The PG distributions were measured for 10 s (6.25×10^{10} protons) of beam irradiation. As shown in Fig. 8, The range of the proton beam in the PMMA phantom confirmed using EBT film was 17 mm, but the range of the proton beam confirmed through Geant4 simulation and PG imaging acquisition was evaluated as 16 mm. This 1 mm difference is expected to be due to the variation in the photosensitivity of the film in which the conditions at the time of the experiment were comprehensively expressed [31,32]. The intensity of the PG distribution in relation to the depth direction was rap idly decreased at a depth of 16 mm from the surface, near the position of the Bragg peak. Regarding the lateral distribution, the intensity of the PG distribution was steeply increased in the 20 mm diameter around the center of the proton dose distribution. Based on the results of the PG distribution measurements, we report herein that 6.25×10^{10} protons are sufficient to clearly discriminate a PG distribution. However, further study is necessary in order to quantitatively evaluate the minimal proton fluence with the higher proton energies routinely used in clinics.

3.2.3. Positron emitter (PE) distribution

The PE distributions for the 45 MeV proton beam were estimated according to the coincidence projection images of 511 keV gammas reconstructed using the MLEM algorithm implemented in the CASToR software. The coincidence events were processed for events only in the 511 keV peak region in the channels' energy spectra. The time resolution for the coincidence events was 3.6 ns for a distance of 752 mm between the centres of the two GAGG scintillator arrays.

The measured PE distributions showed that the PE was densely concentrated near the dose fall-off region. As shown in Fig. 9, the intensity of the PE distribution was sharply increased at 4 mm from the entrance surface of the phantom. Although the peak position of the distribution was at a depth of 12 mm, there was a rapidly decreased at a depth of 16 mm, showing a distribution to the Gaussian peak distribution. The lateral PE distribution showed a

Table 1
Energy resolutions measured in scintillator pixels of dual-head PG-PET system for four gamma energies.

	356 keV		511 keV		662 keV		1275 keV	
	Det.1	Det.2	Det.1	Det.2	Det.1	Det.2	Det.1	Det.2
Energy resolution (%)	15.4 ± 2.8	17.3 ± 3.1	12.7 ± 1.1	14.3 ± 3.3	11.4 ± 1.4	13.1 ± 3.1	3.5 ± 2.2	5.2 ± 3.6

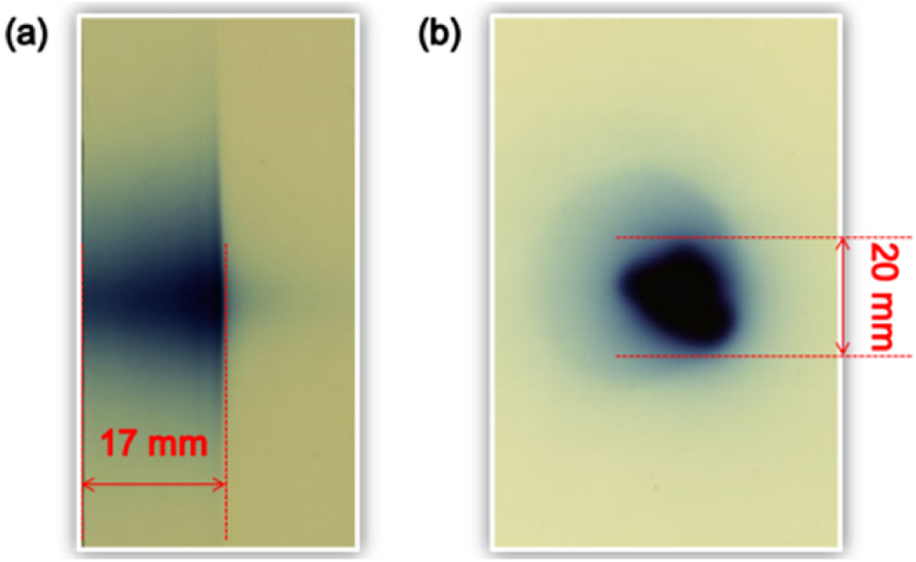

Fig. 6. (a) Depth dose distribution of 45 MeV proton beam measured by EBT3 film at central plane of PMMA phantom, (b) lateral dose distribution of 45 MeV proton beam on surface of PMMA phantom.

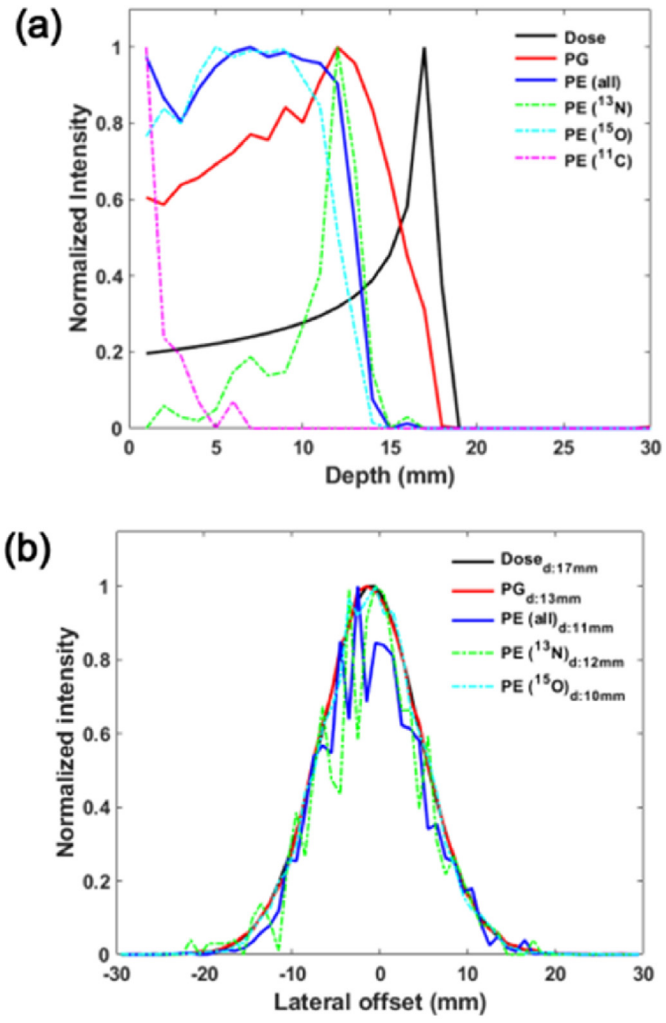

Fig. 7. Proton dose distribution and generation distributions of PG and PE (a) in longitudinal direction and (b) lateral direction by Monte Carlo method.

Gaussian peak shape with a FWHM of about 12 mm. The peak position was located slightly above the center of the PG distribution, just like the distribution of the width of the lateral dose distribution. While the lateral distribution diameter of 13 N calculated by the MC method was 12 mm and the peak position was 13 mm, the measured lateral distribution and peak position were 12 mm and 16 mm, respectively (Fig. 7). Although there was a 3 mm difference in peak position, based on the experimental results of PE distribution measurement, we assumed that PE distribution, owing to its higher spatial resolution, could better estimate a more realistic lateral dose distribution than PG distribution.

4. Conclusion

Based on the MC simulation study previously conducted to design the integrated PG-PET imaging system, the PG-PET system was constructed for a proof-of-principle study using a 45 MeV proton beam. We successfully obtained PG and PE distributions with a dual-head detection system. The experimental results for the PG-PET system demonstrated that the PG distribution can be measured simply by combining the 2-D parallel-hole collimator and the PET detector module. Furthermore, the results showed that the PG and PE distributions have advantages for estimating the proton range and the lateral shape of the dose distribution, respectively.

However, the proton beam nozzle employed in clinics uses a beam of 60–220 MeV energy and 0–40 nA intensity, which is higher than the KIRAMS beam of 45 MeV energy and 1 nA intensity. The amount of background radiation, including the neutrons, would also be higher because the proton energy is higher. To address this point, a collimation system filled with low-density materials with a high portion of hydrogen for neutron shielding will be studied in the future.

Moreover, an accurate 3-D dose evaluation technique may also be applied to this system for various proton energies using deep-learning algorithms based on dose, PG, and PE distribution image sets acquired using the MC method. Through an additional study considering the limitations of the current study, mentioned above, we expect that the proposed PG-PET system will further improve treatment quality by realizing a more efficient workflow for adaptive proton therapy.

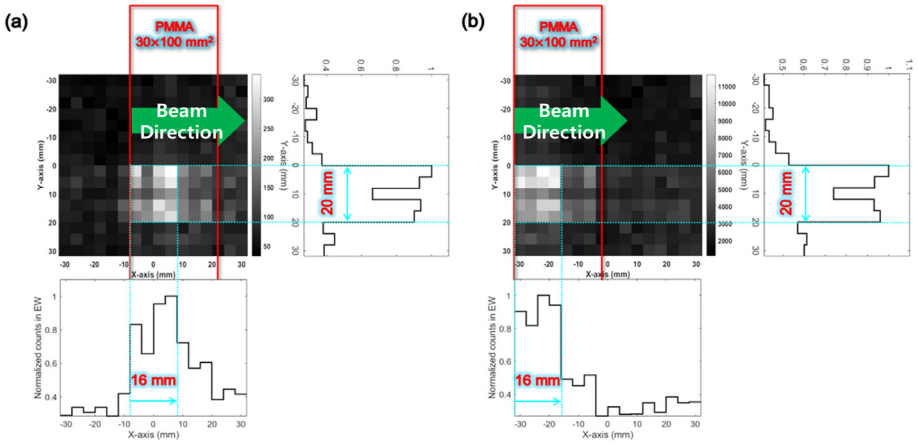

Fig. 8. PG distributions for 45 MeV proton beam, as measured for two different positions of PMMA phantom: (a) phantom located in center of collimator, (b) phantom located at the edge to the beam nozzle side of the collimator.

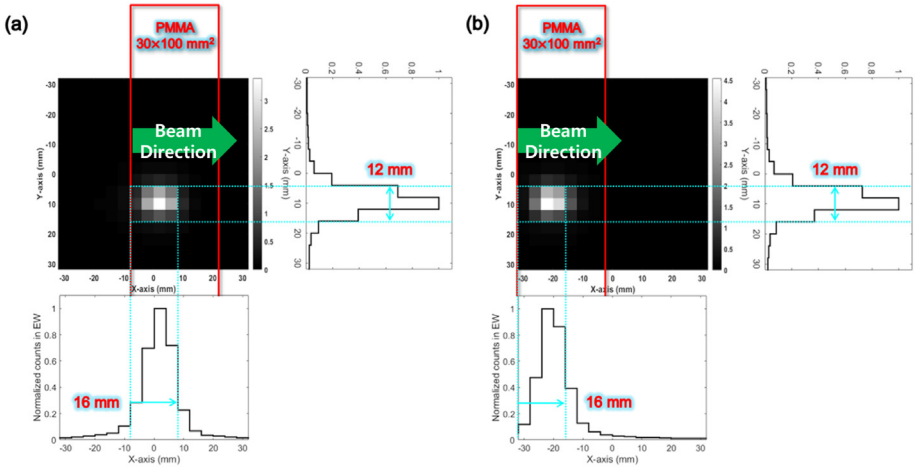

Fig. 9. Coincidence projection images of 511 keV gammas for 45 MeV proton beam reconstructed by MLEM algorithm, as measured for two different positions of PMMA phantom: (a) phantom located in center of field-of-view of collimator, (b) phantom located at the edge to the beam nozzle side of the collimator.

Declaration of competing interest

The authors declare that they have no known competing financial interests or personal relationships that could have appeared to influence the work reported in this paper.

Acknowledgements

This research was supported by National Research Foundation of Korea (NRF); Ministry of Science, ICT, and Future Planning (2020R1A2C201157613), "Regional Innovation Strategy (RIS)" through the National Research Foundation of Korea(NRF) funded by the Ministry of Education(MOE) (2022RIS-005), and Korea Institute of Energy Technology Evaluation and Planning (KETEP) grant funded by the Korea government (MOTIE) (G032579811).

References

[1] J Applied Clin Med Phys, Choi - Development of a Geant4-based Independent Patient Dose Validation System with an.Pdf, 2019 (n.d.).
[2] W.P. Levin, H. Kooy, J.S. Loeffler, T.F. DeLaney, Proton beam therapy, Br. J. Cancer 93 (2005) 849–854, https://doi.org/10.1038/sj.bjc.6602754.
[3] R. Miralbell, A. Lomax, L. Cella, U. Schneider, Potential reduction of the incidence of radiation-induced second cancers by using proton beams in the treatment of pediatric tumors, Int. J. Radiat. Oncol. Biol. Phys. 54 (2002) 824–829, https://doi.org/10.1016/S0360-3016(02)02982-6.
[4] K. Otto, Volumetric modulated arc therapy: IMRT in a single gantry arc, Med. Phys 35 (2008) 310–317, https://doi.org/10.1118/1.2818738.
[5] R.R. Wilson, Radiological use of fast protons, Radiology 47 (1946) 487–491, https://doi.org/10.1148/47.5.487.
[6] A.C. Knopf, A. Lomax, In vivo proton range verification: a review, Phys. Med. Biol. 58 (2013) 131–160, https://doi.org/10.1088/0031-9155/58/15/R131.
[8] F. Albertini, E.B. Hug, A.J. Lomax, The influence of the optimization starting conditions on the robustness of intensity-modulated proton therapy plans, Phys. Med. Biol. 55 (2010) 2863–2878, https://doi.org/10.1088/0031-9155/55/10/005.
[9] H.H. Lin, H.T. Chang, T.C. Chao, K.S. Chuang, A comparison of two prompt gamma imaging techniques with collimator-based cameras for range verification in proton therapy, Radiat. Phys. Chem. 137 (2017) 144–150, https://doi.org/10.1016/j.radphyschem.2016.04.020.
[10] C. Golnik, F. Hueso-González, A. Müller, P. Dendooven, W. Enghardt, F. Fiedler, T. Kormoll, K. Roemer, J. Petzoldt, A. Wagner, G. Pausch, Range assessment in particle therapy based on prompt γ-ray timing measurements, Phys. Med. Biol. 59 (2014) 5399–5422, https://doi.org/10.1088/0031-9155/59/18/5399.
[11] J. Krimmer, D. Dauvergne, J.M. Létang, Testa, Prompt-gamma monitoring in hadrontherapy: a review, Nucl. Instruments Methods Phys. Res. Sect. A Accel. Spectrometers, Detect. Assoc. Equip. 878 (2018) 58–73, https://doi.org/10.1016/j.nima.2017.07.063.
[12] P. Cambraia Lopes, P. Crespo, J. Huizenga, D.R. Schaart, Optimization of the signal-to-background ratio in prompt gamma imaging using energy and shifting time-of-flight discrimination: experiments with a scanning parallel-slit collimator, IEEE Trans. Radiat. Plasma Med. Sci. 2 (2018) 510–519, https://doi.org/10.1109/TRPMS.2018.2846612.
[13] C.H. Min, C.H. Kim, M.Y. Youn, J.W. Kim, Prompt gamma measurements for

locating the dose falloff region in the proton therapy, Appl. Phys. Lett. 89 (2006) 2–5, https://doi.org/10.1063/1.2378561.
[14] C. Richter, G. Pausch, S. Barczyk, M. Priegnitz, I. Keitz, J. Thiele, J. Smeets, F. Vander Stappen, L. Bombelli, C. Fiorini, L. Hotoiu, I. Perali, D. Prieels, W. Enghardt, M. Baumann, First clinical application of a prompt gamma based in vivo proton range verification system, Radiother. Oncol. 118 (2016) 232–237, https://doi.org/10.1016/j.radonc.2016.01.004.
[15] J.M. Verburg, K. Riley, T. Bortfeld, J. Seco, Energy- and time-resolved detection of prompt gamma-rays for proton range verification, Phys. Med. Biol. 58 (2013), https://doi.org/10.1088/0031-9155/58/20/L37.
[16] Y. Xie, E.H. Bentefour, G. Janssens, J. Smeets, F. Vander Stappen, L. Hotoiu, L. Yin, D. Dolney, S. Avery, F. O'Grady, D. Prieels, J. McDonough, T.D. Solberg, R.A. Lustig, A. Lin, B.K.K. Teo, Prompt gamma imaging for in vivo range verification of pencil beam scanning proton therapy, Int. J. Radiat. Oncol. Biol. Phys. 99 (2017) 210–218, https://doi.org/10.1016/j.ijrobp.2017.04.027.
[17] W. Enghardt, P. Crespo, F. Fiedler, R. Hinz, K. Parodi, J. Pawelke, F. Pönisch, Charged hadron tumour therapy monitoring by means of PET, Nucl. Instruments Methods Phys. Res. Sect. A Accel. Spectrometers, Detect. Assoc. Equip. 525 (2004) 284–288, https://doi.org/10.1016/j.nima.2004.03.128.
[18] V. Ferrero, E. Fiorina, M. Morrocchi, F. Pennazio, G. Baroni, G. Battistoni, N. Belcari, N. Camarlinghi, M. Ciocca, A. Del Guerra, M. Donetti, S. Giordanengo, G. Giraudo, V. Patera, C. Peroni, A. Rivetti, M.D.D.R. Rolo, S. Rossi, V. Rosso, G. Sportelli, S. Tampellini, F. Valvo, R. Wheadon, P. Cerello, M.G. Bisogni, Online proton therapy monitoring: clinical test of a Silicon-photodetector-based in-beam PET, Sci. Rep. 8 (2018) 1–8, https://doi.org/10.1038/s41598-018-22325-6.
[19] P. Cambraia Lopes, J. Bauer, A. Salomon, I. Rinaldi, V. Tabacchini, T. Tessonnier, P. Crespo, K. Parodi, D.R. Schaart, First in situ TOF-PET study using digital photon counters for proton range verification, Phys. Med. Biol. 61 (2016) 6203–6230, https://doi.org/10.1088/0031-9155/61/16/6203.
[20] S.F. Kry, B. Bednarz, R.M. Howell, L. Dauer, D. Followill, E. Klein, H. Paganetti, B. Wang, C.S. Wuu, X. George Xu, M.C. Alves, W.S. Santos, C. Lee, W.E. Bolch, J.G. Hunt, A.B. Carvalho Junior, M. Jacquet, S. Marcatili, M.L. Gallin-Martel, J.L. Bouly, Y. Boursier, D. Dauvergne, M. Dupont, L. Gallin-Martel, J. Hérault, J.M. Létang, D. Manéval, C. Morel, J.F. Muraz, É. Testa, K. Busch, A.G. Andersen, J.B.B. Petersen, S.E. Petersen, S. Heidi, M. Fang, Y. Altmann, D. Della Latta, M. Salvatori, A. Di Fulvio, H. Si, Y.S. Yeom, J.H. Jeong, M.C. Han, C.H. Kim, H.S. Kim, T.T. Nguyen, C. Choi, M.C. Han, C.H. Kim, J.K. Lee, M. Zankl, N. Petoussi-Henss, W.E. Bolch, C. Lee, B.S. Chung, New small-intestine modeling method for surface-based computational human phantoms, ArXiv 36 (2017), https://doi.org/10.1093/rpd/ncw271 e391–e429.
[21] M. Moteabbed, S. España, H. Paganetti, Monte Carlo patient study on the comparison of prompt gamma and PET imaging for range verification in proton therapy, Phys. Med. Biol. 56 (2011) 1063–1082, https://doi.org/10.1088/0031-9155/56/4/012.
[22] T. Nishio, A. Miyatake, T. Ogino, K. Nakagawa, N. Saijo, H. Esumi, The development and clinical use of a beam ON-LINE PET system mounted on a rotating gantry port in proton therapy, Int. J. Radiat. Oncol. Biol. Phys. 76 (2010) 277–286, https://doi.org/10.1016/j.ijrobp.2009.05.065.
[23] H. Tashima, T. Yamaya, E. Yoshida, S. Kinouchi, M. Watanabe, E. Tanaka, A single-ring OpenPET enabling PET imaging during radiotherapy, Phys. Med. Biol. 57 (2012) 4705–4718, https://doi.org/10.1088/0031-9155/57/14/4705.
[24] H. Tashima, E. Yoshida, N. Inadama, F. Nishikido, Y. Nakajima, H. Wakizaka, T. Shinaji, M. Nitta, S. Kinouchi, M. Suga, H. Haneishi, T. Inaniwa, T. Yamaya, Development of a small single-ring OpenPET prototype with a novel transformable architecture, Phys. Med. Biol. 61 (2016) 1795–1809, https://doi.org/10.1088/0031-9155/61/4/1795.
[25] X. Zhu, G. El Fakhri, Proton therapy verification with PET imaging, Theranostics 3 (2013) 731–740, https://doi.org/10.7150/thno.5162.
[26] H.J. Choi, J.W. Jang, W.G. Shin, H. Park, S. Incerti, C.H. Min, Development of integrated prompt gamma imaging and positron emission tomography system for in vivo 3-D dose verification: a Monte Carlo study, Phys. Med. Biol. 65 (2020), https://doi.org/10.1088/1361-6560/ab857c.
[27] C. Kim, J.-Y. Yeom, G. Kim, Digital n-γ pulse shape discrimination in organic scintillators with a high-speed digitizer, J. Radiat. Prot. Res. 44 (2019) 53–63, https://doi.org/10.14407/jrpr.2019.44.2.53.
[28] R. Bugalho, A. Di Francesco, L. Ferramacho, C. Leong, T. Niknejad, L. Oliveira, L. Pacher, M. Rolo, A. Rivetti, M. Silveira, J.C. Silva, R. Silva, S. Tavernier, J. Varela, Experimental results with TOFPET2 ASIC for time-of-flight applications, Nucl. Instruments Methods Phys. Res. Sect. A Accel. Spectrometers, Detect. Assoc. Equip. 912 (2018) 195–198, https://doi.org/10.1016/j.nima.2017.11.034.
[29] T. Merlin, S. Stute, D. Benoit, J. Bert, T. Carlier, C. Comtat, M. Filipovic, F. Lamare, D. Visvikis, CASToR: a generic data organization and processing code framework for multi-modal and multi-dimensional tomographic reconstruction, Phys. Med. Biol. 63 (2018), https://doi.org/10.1088/1361-6560/aadac1, 0–15.
[30] S. Agostinelli, J. Allison, K. Amako, J. Apostolakis, H. Araujo, P. Arce, M. Asai, D. Axen, S. Banerjee, G. Barrand, F. Behner, L. Bellagamba, J. Boudreau, L. Broglia, A. Brunengo, H. Burkhardt, S. Chauvie, J. Chuma, R. Chytracek, G. Cooperman, G. Cosmo, P. Degtyarenko, A. Dell'Acqua, G. Depaola, D. Dietrich, R. Enami, A. Feliciello, C. Ferguson, H. Fesefeldt, G. Folger, F. Foppiano, A. Forti, S. Garelli, S. Giani, R. Giannitrapani, D. Gibin, J.J. Gomez Cadenas, I. Gonzalez, G. Gracia Abril, G. Greeniaus, W. Greiner, V. Grichine, A. Grossheim, S. Guatelli, P. Gumplinger, R. Hamatsu, K. Hashimoto, H. Hasui, A. Heikkinen, A. Howard, V. Ivanchenko, A. Johnson, F.W. Jones, J. Kallenbach, N. Kanaya, M. Kawabata, Y. Kawabata, M. Kawaguti, S. Kelner, P. Kent, A. Kimura, T. Kodama, R. Kokoulin, M. Kossov, H. Kurashige, E. Lamanna, T. Lampen, V. Lara, V. Lefebure, F. Lei, M. Liendl, W. Lockman, F. Longo, S. Magni, M. Maire, E. Medernach, K. Minamimoto, P. Mora de Freitas, Y. Morita, K. Murakami, M. Nagamatu, R. Nartallo, P. Nieminen, T. Nishimura, K. Ohtsubo, M. Okamura, S. O'Neale, Y. Oohata, K. Paech, J. Perl, A. Pfeiffer, M.G. Pia, F. Ranjard, A. Rybin, S. Sadilov, E. di Salvo, G. Santin, T. Sasaki, N. Savvas, Y. Sawada, S. Scherer, S. Sei, V. Sirotenko, D. Smith, N. Starkov, H. Stoecker, J. Sulkimo, M. Takahata, S. Tanaka, E. Tcherniaev, E. Safai Tehrani, M. Tropeano, P. Truscott, H. Uno, L. Urban, P. Urban, M. Verderi, A. Walkden, W. Wander, H. Weber, J.P. Wellisch, T. Wenaus, D.C. Williams, D. Wright, T. Yamada, H. Yoshida, D. Zschiesche, GEANT4 - a simulation toolkit, Nucl. Instruments Methods Phys. Res. Sect. A Accel. Spectrometers, Detect. Assoc. Equip. 506 (2003) 250–303, https://doi.org/10.1016/S0168-9002(03)01368-8.
[31] M.C. Battaglia, D. Schardt, J.M. Espino, M.I. Gallardo, M.A. Cortés-Giraldo, J.M. Quesada, A.M. Lallena, H. Miras, D. Guirado, Dosimetric response of radiochromic films to protons of low energies in the Bragg peak region, Phys. Rev. Accel. Beams. 19 (2016) 1–7, https://doi.org/10.1103/PhysRevAccelBeams.19.064701.
[32] J. Sorriaux, A. Kacperek, S. Rossomme, J.A. Lee, D. Bertrand, S. Vynckier, E. Sterpin, Evaluation of Gafchromic® EBT3 films characteristics in therapy photon, electron and proton beams, Phys. Med. 29 (2013) 599–606, https://doi.org/10.1016/j.ejmp.2012.10.001.